# A thermal network model for induction motors of hermetic reciprocating compressors

**T Dutra, C J Deschamps**[1]
POLO Research Laboratories for Emerging Technologies in Cooling and Thermophysics, Federal University of Santa Catarina, Florianopolis, SC, Brazil

E-mail: deschamps@polo.ufsc.br

**Abstract.** This paper describes a simulation model for small reciprocating compressors with emphasis on the electrical motor modelling. Heat transfer is solved through algebraic equations derived from lumped thermal energy balances applied to the compressor components. Thermal conductances between the motor components are characterized via a thermal network model. The single-phase induction motor is modelled via an equivalent circuit, allowing predictions for the motor performance and distributed losses. The predicted temperature distribution is used to evaluate the stator and rotor windings resistances. The thermal and electric models are solved in a coupled manner with a model for the compression cycle. Predictions of temperature distribution, motor efficiency, as well as isentropic and volumetric efficiencies, are compared with experimental data at different operating conditions. The model is then applied to analyse the motor temperature as a function of input voltage and stator wire diameter.

## 1. Introduction

The development of simulation models is of major importance to design more efficient and reliable compressors, requiring modelling approaches to predict the compression cycle, temperature distribution and electrical motor performance. The compression cycle can be modelled based on polytropic processes [1], lumped-parameter models [2] or distributed-parameter models [3]. On the other hand, the temperature distribution inside the compressor has been usually predicted via lumped-parameter methods and thermal conductances to characterize heat transfer between the components. Several models [2] divide the compressor domain into a few control volumes and employ global conductances obtained from experimental data, whereas other models [4] use thermal network approaches (TNW). TNW models usually adopt a greater division of the compressor domain, allowing the prediction of a more detailed temperature distribution. Finally, full finite volume models [3] and hybrid models [5] have also been developed for compressor thermal simulation.

The electrical motor is usually taken into account in compressor simulations through experimental relationships between torque, efficiency and speed [3, 6]. Few works consider an electrical model for the driving motor [7-9]. He *et al.* [8] presented a simulation model for a semi-hermetic screw compressor combining a TNW approach with an electrical circuit for a three-phase induction motor. The authors validated their model and analysed the temperature distribution as a function of the motor geometrical parameters. Dutra and Deschamps [7] presented a simulation model for a hermetic reciprocating compressor employing lumped-parameter approaches for the thermal and electrical sub-

[1] To whom any correspondence should be addressed.

models, respectively. Predictions were validated through comparisons with measurements of compressor efficiency and components temperatures at different operating conditions.

The present paper presents a simulation model similar to that of Dutra and Deschamps [7]. However, instead of a lumped formulation to predict a single temperature to characterize the electrical motor, a TNW approach is adopted to calculate the temperatures of different motor components. Therefore, a more detailed thermal characterization of the electrical motor is achieved with no significant increase of the computational cost. The proposed model is validated through comparisons with measurements and then a parametric study is carried out to illustrate its application, by analysing the effect of the stator main winding diameter on the motor temperature distribution.

## 2. Mathematical model

### *2.1. Compression cycle model*

An unsteady-state lumped formulation was employed for the compression chamber modelling [10], resulting the following equations for the variations of mass and temperature in the compression chamber:

$$\frac{dm_c}{dt} = \dot{m}_s - \dot{m}_d - \dot{m}_l - \dot{m}_{bs} + \dot{m}_{bd} \tag{1}$$

$$\frac{dT_c}{dt} = \frac{1}{m_c c_v}\left\{\dot{Q}_w - h_c\frac{dm_c}{dt} - \sum \dot{m}h - \left[\frac{T_c}{\rho_c}\left.\frac{\partial p_c}{\partial T_c}\right|_\rho \left(\rho_c\frac{dV_c}{dt} - \frac{dm_c}{dt}\right)\right]\right\} \tag{2}$$

where $t$, $T$, $m$, $c_v$, $\dot{Q}_w$, $V_c$ and $p$ refer respectively to time, temperature, mass, specific heat at constant volume, heat transfer rate through cylinder walls, instantaneous volume of the compression chamber and pressure. Gas properties $h$ and $\rho$ denote specific enthalpy and density. Subscript $c$ stands for compression chamber. Mass flow rate through suction and discharge valves are $\dot{m}_s$ and $\dot{m}_d$, whereas $\dot{m}_{bs}$ and $\dot{m}_{bd}$ correspond to backflows and $\dot{m}_l$ is leakage in the piston-cylinder gap. The aforementioned parameters are evaluated following Link and Deschamps [10]. Equations (1) and (2) are solved via the Runge-Kutta method.

The compression power is calculated from:

$$\dot{W}_c = -\frac{\omega}{2\pi}\oint p_c dV_c \tag{3}$$

where $\omega$ is the compressor speed. The required power to run the compressor is obtained by summing the total mechanical losses in the bearings, $\dot{W}_b$, and the compression power ($\dot{W}_r = \dot{W}_b + \dot{W}_c$). For the compressor considered in the present study, bearing losses are estimated from measurements to be approximately 9W.

### *2.2. Thermal model*

*2.2.1. General formulation.* A steady-state energy balance applied to a generic lumped element $i$ can be expressed as:

$$\dot{Q}_i - \dot{W}_i = \sum(\dot{m}h)_{i,in} - \sum(\dot{m}h)_{i,out} \tag{4}$$

where $\dot{Q}_i$ may represent the heat transfer rate between the element $i$ and its surroundings, or any heat generation rate within this element. The rate of work associated with the element $i$ is $\dot{W}_i$ and the energy advective transport terms into and from the element $i$ are denoted by $\Sigma(\dot{m}h)_{i,in}$ and $\Sigma(\dot{m}h)_{i,out}$.

The reciprocating compressor was divided into eleven elements: suction muffler (1), compression chamber (2), discharge chamber (3), discharge muffler (4), discharge tube (5), internal environment (6), compressor housing (7), stator core (8), stator winding (9), rotor (10) and stator slots/teeth surface (11). A schematic view of the compressor elements and the thermal interaction among them is depicted in figure 1. Axisymmetric and circular sector schematic views concerning only the motor components are shown in figure 2.

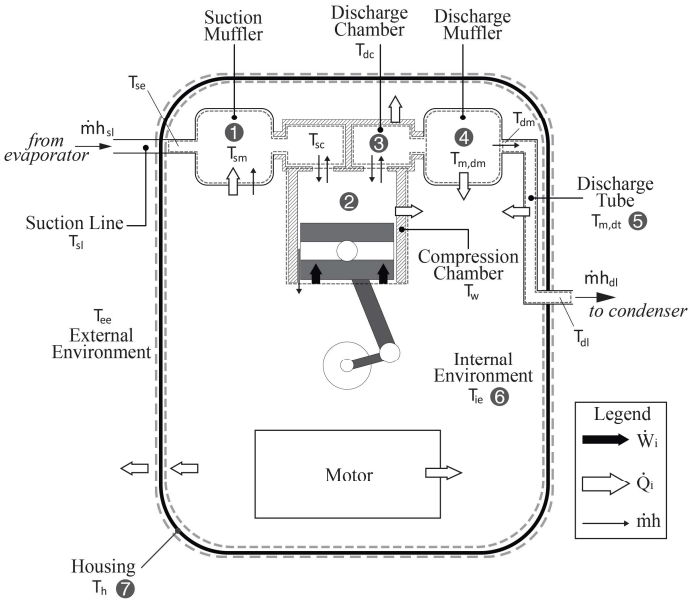


**Figure 1.** Compressor lumped elements.

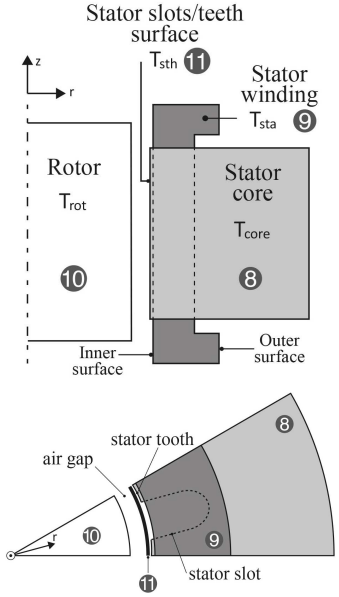


**Figure 2.** Motor elements.

Tables 1 and 2 show the energy balance terms $\dot{Q}$, $\dot{W}$, $\Sigma(\dot{m}h)_{in}$ and $\Sigma(\dot{m}h)_{out}$ associated with each one of the compressor elements defined in the thermal model. Several parameters, such as mass flow and backflow rates ($\dot{m}_s$, $\dot{m}_d$, $\dot{m}_{bs}$, $\dot{m}_{bd}$, $\dot{m}_l$) heat generation rates in components of the electrical motor ($\dot{Q}_{sta}$, $\dot{Q}_{rot}$, $\dot{Q}_{core}$), compression power ($\dot{W}_c$), mechanical losses in bearings ($\dot{W}_b$) and specific enthalpy in the compression chamber ($h_c$) are input data for the thermal simulation. The mass flow rates, compression power and specific enthalpy are obtained from the compression cycle model, whereas the mechanical and electrical losses are obtained from measurements and the electrical model, respectively.

Heat transfer between most of elements inside the compressor is taken into account by introducing global conductances, *UA*. These conductances are determined via temperature measurements at a single operating condition [2] and maintained fixed in thermal simulations under a wide range of operating conditions. Heat transfer between the motor components is modelled via local conductances, *H*, estimated from correlations available in literature for simple geometries. However, heat transfer between the motor components and the internal environment is evaluated by considering both global and local conductances. In such situations, heat transfer associated with global conductances represents an additional energy transfer rate that cannot be predicted by adopting only local conductances for simplified geometries.

The system of non-linear equations is solved via the Newton-Raphson method. The mean temperatures in the suction muffler, discharge muffler and discharge tube, denoted respectively by $T_{sm}$, $T_{m,dm}$ and $T_{m,dt}$, are given by:

$$T_{sm}=0.5(T_{sl}+T_{sc}); \qquad T_{m,dm}=0.5(T_{dc}+T_{dm}); \qquad T_{m,dt}=0.5(T_{dm}+T_{dl}) \tag{5}$$

**Table 1.** Heat transfer rate terms in the energy balances of the thermal model.

| ID | $\dot{Q}$ |
|---|---|
| **1** | $UA_{sm}(T_{sm}-T_{ie})$ |
| **2** | $UA_{w}(T_{w}-T_{ie})$ |
| **3** | $UA_{dc}(T_{dc}-T_{ie})$ |
| **4** | $UA_{dm}\left(T_{m,dm}-T_{ie}\right)$ |
| **5** | $UA_{dt}\left(T_{m,dt}-T_{ie}\right)$ |
| **6** | $H_{rot,ie}(T_{ie}-T_{rot})+H_{sta,ie}(T_{ie}-T_{sta})+H_{core,ie}(T_{ie}-T_{core})+\sum UA_{i}(T_{ie}-T_{i})$ |
| **7** | $UA_{h,ee}(T_{h}-T_{ee})-UA_{h,ie}(T_{ie}-T_{h})$ |
| **8** | $\left(H_{core,ie}+UA_{core}\right)(T_{core}-T_{ie})+H_{core,sth}(T_{core}-T_{sth})-\dot{Q}_{core}$ |
| **9** | $\left(H_{sta,ie}+UA_{sta}\right)(T_{sta}-T_{ie})+H_{sta,sth}(T_{sta}-T_{sth})-\dot{Q}_{sta}$ |
| **10** | $\left(H_{rot,ie}+UA_{rot}\right)(T_{rot}-T_{ie})+H_{rot,sth}(T_{rot}-T_{sth})-\dot{Q}_{rot}$ |
| **11** | $H_{rot,sth}(T_{sth}-T_{rot})+H_{sta,sth}(T_{sth}-T_{sta})+H_{core,sth}(T_{sth}-T_{core})+UA_{sth}(T_{sth}-T_{ie})$ |

**Table 2.** Rate of work and energy advective terms in the energy balances of the thermal model.

| ID | $\dot{W}$ | $\sum \dot{m}h\|_{in}$ | $\sum \dot{m}h\|_{out}$ |
|---|---|---|---|
| **1** | - | $\dot{m}h_{sl}+\dot{m}_{l}h_{ie}+\dot{m}_{bs}h_{c}$ | $\dot{m}_{s}h_{sc}$ |
| **2** | $\dot{W}_{c}+\dot{W}_{b}$ | $\dot{m}_{s}h_{sc}+\dot{m}_{bd}h_{dc}$ | $\dot{m}_{l}h_{c}+\dot{m}_{bs}h_{c}+\dot{m}_{d}h_{c}$ |
| **3** | - | $\dot{m}_{d}h_{c}$ | $\dot{m}_{bd}h_{dc}+\dot{m}h_{dc}$ |
| **4** | - | $\dot{m}h_{dc}$ | $\dot{m}h_{dm}$ |
| **5** | - | $\dot{m}h_{dm}$ | $\dot{m}h_{dl}$ |
| **6** | - | $\dot{m}_{l}h_{c}$ | $\dot{m}_{l}h_{ie}$ |
| **7-11** | - | - | - |

*2.2.2. TNW for motor components.* Heat transfer between the motor components, i.e. rotor, stator winding and stator core, is solved by a TNW approach, commonly adopted to predict the temperature distribution of electrical machines [11, 12]. Local conductances between elements *i* and *j* are computed by combining theoretical estimates of conductive and convective thermal resistances:

$$H_{i,j}=\frac{1}{R_{i,j}};\qquad R_{i,j}^{h}=\frac{1}{hA};\qquad R_{i,j}^{k,z}=\frac{L}{kA};\qquad R_{i,j}^{k,r}=\frac{ln(D_e/D_i)}{2\pi kL} \tag{6}$$

where $h$, $A$, $L$, $k$, $D_e$ and $D_i$ denote the convective heat transfer coefficient, contact surface area, characteristic length, thermal conductivity and outer and inner diameters of lumped elements, respectively. The superscripts $h$ and $k$ refer to convective and conductive resistances, whereas $z$ and $r$ represent axial and radial axes of the coordinate system, respectively. Heat transfer in circumferential direction is neglected. Figure 3 shows the resulting thermal circuit for the induction motor, which is similar to that used by Boglietti *et al.* [12]. The identification (ID) of the motor elements (tables 1 and 2) are used in the subscripts of the thermal resistances. It should be noted that thermal resistances

between the components 8 (stator core) and 10 (rotor) and the internal environment are represented by conductive and convective resistances in series. The conductive resistances $R_{8,6}^{k,r}$, $R_{8,6}^{k,z}$ and $R_{10,6}^{k,z}$ represent the temperature drop within the motor element itself, i.e. between the centre of the element (node) and its border. The convective resistance is associated with heat transfer between the element border and the internal environment.

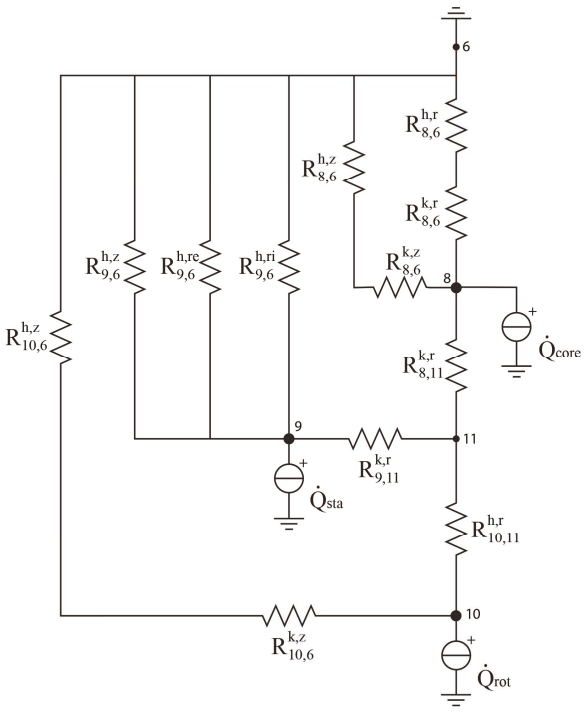


$R_{10,6}^{k,z}$ - Axial conductive resistance between rotor and ie.

$R_{10,6}^{h,z}$ - Axial convective resistance between rotor and ie.

$R_{10,11}^{h,r}$ - Radial convective resistance between rotor and stator slots/teeth surface (air gap).

$R_{8,6}^{h,z}$ - Axial convective resistance between stator core and ie.

$R_{8,6}^{h,r}$ - Radial convective resistance between stator core and ie.

$R_{8,6}^{k,z}$ - Axial conductive resistance between stator core and ie.

$R_{8,6}^{k,r}$ - Radial conductive resistance between stator core and ie.

$R_{8,11}^{k,r}$ - Radial conductive resistance between stator core and stator slots/teeth surface.

$R_{9,6}^{h,z}$– Axial convective resistance between stator winding and ie.

$R_{9,11}^{k,r}$ - Radial conductive resistance between stator winding and stator slots/teeth surface.

$R_{9,6}^{h,re}$ - Radial convective resistance between stator winding and ie (outer surface – figure 2).

$R_{9,6}^{h,ri}$ - Radial convective resistance between stator winding and ie (inner surface, facing the rotor – figure 2).

**Figure 3.** Motor TNW and corresponding thermal resistances label.

One of the most difficult tasks on adopting lumped thermal models based on local conductances is to determine characteristic lengths, contact surface areas and flow velocities for calculation of thermal resistances. Convective resistances are modelled with reference to local heat transfer coefficients computed from correlations available in literature. For instance, a correlation for turbulent flow over a flat plate is considered for the convective resistances $R_{9,6}^{h,z}$, $R_{9,6}^{h,re}$, $R_{9,6}^{h,ri}$, $R_{8,6}^{h,z}$ and $R_{8,6}^{h,r}$ between stator components and internal environment:

$$h=\frac{Nu_L k}{L}; \quad Nu_L=0.037Re_L^{0.8}Pr^{0.33}; \quad Re_L=\frac{\rho VL}{\mu}; \quad Pr=\frac{\mu c_p}{k} \tag{7}$$

where $Nu_L$, $Re_L$ and $Pr$ are the Nusselt number, Reynolds number and Prandtl number. Gas properties, such as density, $\rho$, specific heat at constant pressure, $c_p$, dynamic viscosity, $\mu$, and thermal conductivity, $k$, are evaluated at the film temperature corresponding to the average between the temperatures of the motor component and internal environment. The velocity characteristic $V$ is assumed to be a fraction of the crankshaft tangential velocity and $L$ is the length in the flow direction, as proposed by Sanvezzo Jr. and Deschamps [5]. The remaining convective resistances $R_{10,6}^{h,z}$ and $R_{10,11}^{h,r}$ are calculated from correlations available for rotating discs [5] and flow in annular gaps [13], respectively.

*2.3. Electrical model*

The electrical motor operation was modelled with the equivalent circuit method. Figure 4 depicts the circuit of a single-phase induction motor operating at steady-state condition [14]. Such a circuit consists on a set of impedances for the stator, rotor and magnetization; $Z_{sta}$, $Z_{rot}$, $Z_m$, respectively. Impedances are given by combined electrical resistances, $R$, and reactances, $X$. In figure 4, the symbols (+) and (-) represent forward and backward loops, following the theory of rotating magnetic fields.

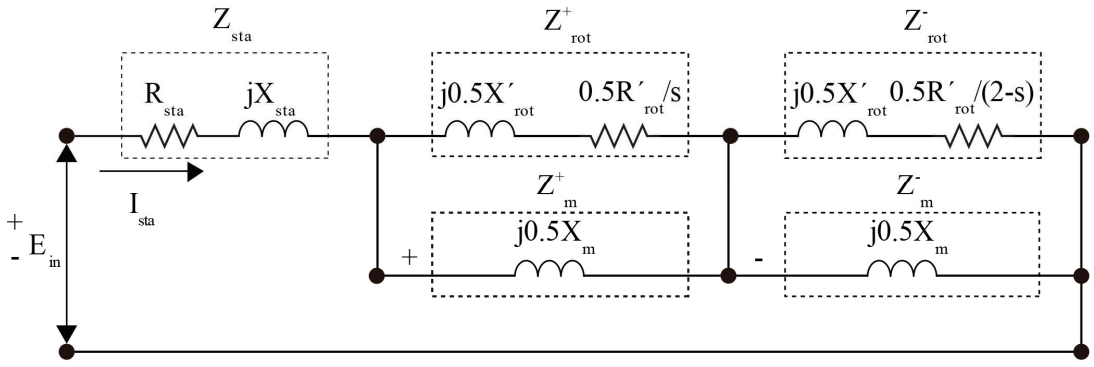


**Figure 4.** Equivalent circuit of a single-phase induction motor at steady state condition.

The solution of the motor equivalent circuit gives the electrical currents in all the branches [7], which allows the calculation of the torque supplied by the motor to the compressor shaft, $\tau_{sh}$, as well as the joule-losses in the stator, $\dot{Q}_{sta}$, and in the rotor windings, $\dot{Q}_{rot}$:

$$\tau_{sh}=\left(\frac{P}{2}\right)\frac{\dot{W}_{sh}}{\omega};\qquad \dot{Q}_{sta}=I_{sta}^2R_{sta};\qquad \dot{Q}_{rot}=0.5\left(I_{rot}^{+\,2}+I_{rot}^{-\,2}\right)R_{rot}^{'} \tag{8}$$

where superscript ´ indicates the rotor resistance is referred to the stator side [14], $P$ is the number of poles and $I_{sta}, I_{rot}^{+}$ and $I_{\bar{r}ot}$ are the electrical currents in the stator winding and rotor forward and backward branches, respectively. The shaft power, $\dot{W}_{sh}$, is evaluated by:

$$\dot{W}_{sh}=(1\text{-}s)\left(I_{rot}^{+\,2}\frac{0.5R_{rot}^{'}}{s}-I_{rot}^{-\,2}\frac{0.5R_{rot}^{'}}{2\text{-}s}\right)-\dot{Q}_{core} \tag{9}$$

where the first and second terms on the right-hand side are the rotating magnetic field power [14] and the stator core loss, $\dot{Q}_{core}$, respectively. The latter is computed from estimates of magnetic flux densities in different regions of the stator core [15]. The solution of equation (9) depends on the slip ratio $s$, which is obtained by substituting equation (9) in the following equation:

$$\dot{W}_{sh}-\dot{W}_r=0 \tag{10}$$

where $\dot{W}_r=\dot{W}_b+\dot{W}_c$.

Equation (10) provides the coupling between the compression cycle model and the electrical model, expressing that the power required to run the compressor is equal to the motor shaft power. This equation is solved via an incremental search technique [16]. Once the shaft power and electrical losses are calculated, the compressor input power and motor efficiency are obtained:

$$\dot{W}=\dot{W}_{sh}+\dot{Q}_{sta}+\dot{Q}_{rot}+\dot{Q}_{core};\qquad \eta_{ele}=\frac{\dot{W}_{sh}}{\dot{W}} \tag{11}$$

The input data for the electrical model are input voltage, $E_{in}$, compressor speed, motor geometry and material properties. The latter two are employed to estimate reference values for electrical resistances and reactances through analytical relations [15]. The electrical resistances are continuously calculated during the simulation by using updated temperatures of motor components:

$$R=R_0+\beta R_0(T-T_0) \tag{12}$$

where subscript $0$ refers to the reference state defined for motor temperature of 25°C and $\beta$ is the temperature coefficient, which is a thermal property of the material. Details of the coupled solution procedure, encompassing compression cycle model, thermal model and electrical model are available in Dutra and Deschamps [7].

## 3. Results and discussions

A R-290 reciprocating compressor designed for household and light commercial applications was considered in this study. The compressor was instrumented with temperature sensors and was run at nine operating conditions, represented by the combination of evaporating temperatures (-10°C, -23.3°C, -35°C) and condensing temperatures (45°C, 54.4°C, 70°C). Each operating condition was tested four times in order to assess the repeatability uncertainty. Compressor external environment temperature, $T_{ee}$, and suction line temperature, $T_{sl}$, were set to (32 ±1)°C. Input voltage and nominal frequency were (228 ±1.2)V and 50Hz, respectively. Measurement uncertainties are ±1% for mass flow rate and compressor input power and ±2°C for temperatures, considering a 95% confidence interval.

The volumetric efficiency, $\eta_v$, is defined as the ratio between the actual mass flow rate and the ideal mass flow rate, whereas the isentropic efficiency, $\eta_s$, is given by the ratio between the isentropic compression power and the actual input power:

$$\eta_v=\frac{\dot{m}}{\dot{m}_{th}}; \qquad \eta_s=\frac{\dot{m}\Delta h_s}{\dot{W}} \tag{13}$$

Results of volumetric and isentropic efficiencies as a function of operating conditions are shown in figures 5 and 6. As can be seen, predictions follow the same trend of experimental data, presenting higher deviations when the pressure ratio is far from that adopted in the calibration condition (-23.3°C/54.4°C). Volumetric efficiency is overestimated and underestimated at -10°C and -35°C evaporating temperatures, respectively. Such an inaccuracy in the mass flow rate prediction affects the isentropic efficiency calculation, which partially explains the deviations found at the same operating conditions. Additionally, inaccuracy related to the input power prediction also increases deviations, especially at the evaporating temperature of -10°C. In this condition, viscous friction in the suction and discharge systems are greater, but the present approach has no specific model for the fluid flow through mufflers to account for this increase. Despite the underlined differences, predictions are considered satisfactory, with maximum deviations of 5.3% and 5.6% for volumetric and isentropic efficiencies.

Volumetric and isentropic efficiencies are decreased by the gas superheating along the compressor suction path. Therefore, the prediction of both parameters requires the calculation of temperatures in the suction chamber and at the cylinder wall. Figure 7 shows results of both temperatures as a function of the operating condition. Predictions become shifted in relation to the measurements when the evaporating temperature is varied. This is likely due to the adoption of fixed global conductances for the thermal model regardless the mass flow rate, which is strongly affected by the evaporating temperature. Despite this shortcoming, the maximum deviation between predictions and measurements is lower than 10°C and most deviations are within 5°C.

Temperatures of motor components are key parameters to be considered in compressor reliability analysis. Figure 8 presents stator winding and core temperature variations with operating conditions.

The maximum difference between predictions and experimental data is approximately 4°C at the operating condition (-10°C /45°C). Measurements indicate that the stator winding temperature is slightly higher (≅ 3°C) than the core temperature. The proposed model also indicates similar results, with smaller differences (<1.8°C) for high evaporating temperatures and greater differences (>4.5°C) for low evaporating temperatures, almost within measurement uncertainties.

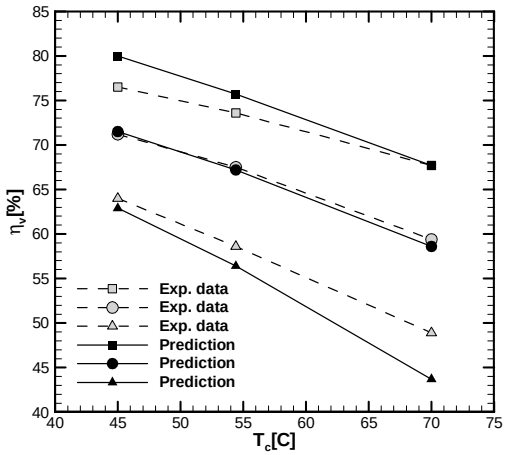


**Figure 5.** Influence of operating condition on volumetric efficiency: ■ $T_e$ = -10°C; ●$T_e$ = -23.3°C; ▲$T_e$ = -35°C.

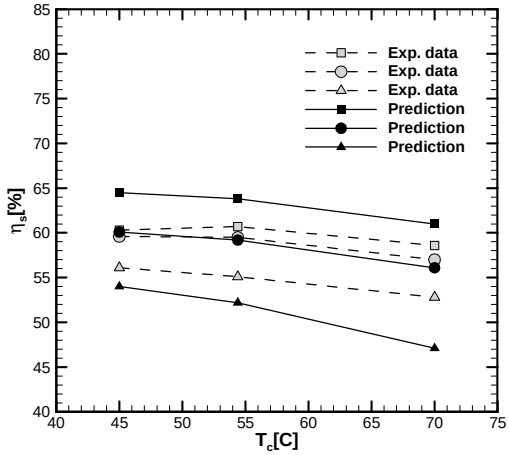


**Figure 6.** Influence of operating condition on isentropic efficiency: ■ $T_e$ = -10°C; ●$T_e$ = -23.3°C; ▲$T_e$ = -35°C.

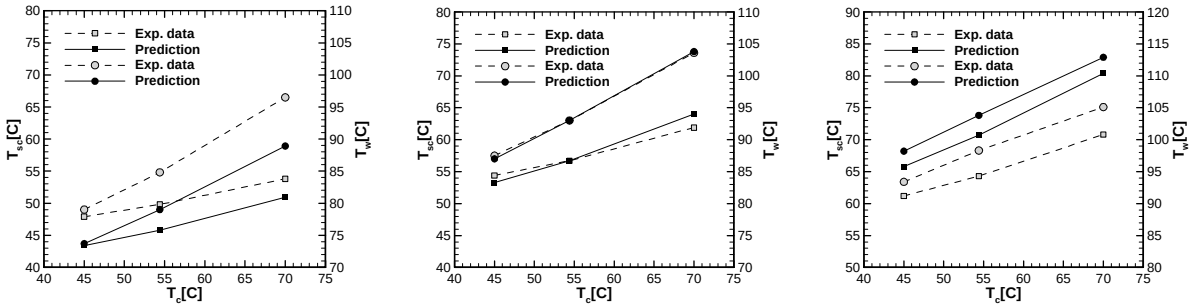


(a) -10°C (b) -23.3°C (c) -35.0°C

**Figure 7.** Suction chamber and cylinder wall temperatures: ■ suction chamber; ● cylinder wall.

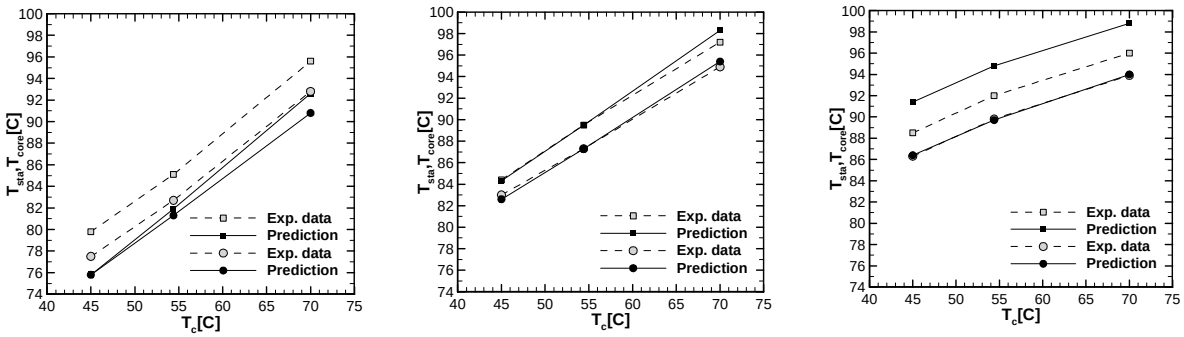


(a) -10°C (b) -23.3°C (c) -35.0°C

**Figure 8.** Motor components temperatures: ■ stator winding; ● stator core.

After its preliminary assessment, the model was applied for parametric analysis. First, the compressor was simulated for a low evaporating temperature condition (-35°C/45°C) and two input voltages (228V and 255V). Figure 9 shows that predictions and measurements are in reasonable agreement, with both results indicating an increase of temperature with the input voltage due to the increase of motor losses. Actually, stator joule-losses ($\dot{Q}_{sta}$) and core losses ($\dot{Q}_{core}$) are found to increase by 5% and 30%, respectively, decreasing the motor efficiency. For instance, figure 10 exhibits results of motor efficiency as a function of shaft torque for input voltages of 220V and 255V. Experimental results obtained with a dynamometer test are also plotted for the purpose of comparison. As can be clearly noted, the motor efficiency is reduced with input voltage increase at the low shaft torque conditions, e.g. -35°C/45°C ($\tau_{sh}$ = 0.28N.m).

Finally, the temperatures of the motor components were analysed as a function of the stator wire diameter for the operating condition (-35°C /45°C). The results depicted in figure 11 indicate the temperatures of the motor components rise when the wire diameter is reduced. This is an expected outcome, since the electrical resistance of the stator winding ($R_{sta}$) is increased, increasing the joule-losses. Hence, the temperature of the stator winding becomes much higher than temperature of the core as the wire diameter is reduced.

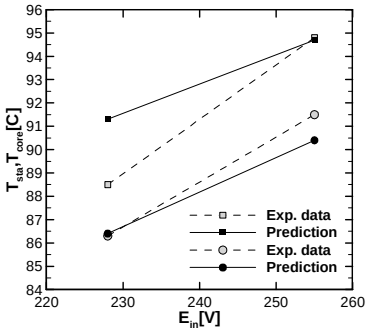


**Figure 9.** Temperature of the motor for different input voltages: ■ stator winding; ● stator core.

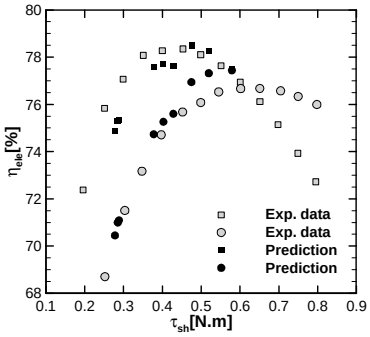


**Figure 10.** Electrical motor efficiency for different shaft torques: ■ 220V; ●255V.

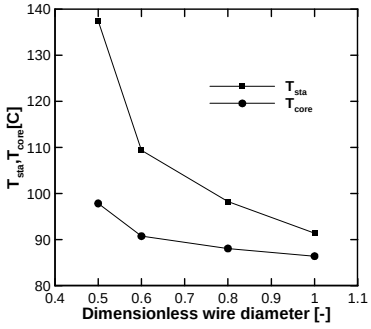


**Figure 11.** Temperature of the motor for different stator wire diameters.

## 4. Conclusions

This paper presented a multi-physic simulation model for hermetic reciprocating compressors adopted for refrigeration. In addition to models for the compression cycle and heat transfer between the compressor components, an approach based on the electrical equivalent circuit was employed for the induction motor. Heat transfer in the electrical motor was modelled via the thermal network concept, with thermal resistances being calculated from analytical and empirical relations. The comprehensive model provided satisfactory predictions for the compressor volumetric and isentropic efficiencies, as well as for the temperature distribution as a function of different operating conditions. The model was also applied in parametric analyses for the motor temperature as a function of input voltage and stator wire diameter.

## Acknowledgments

This study was developed as part of a technical-scientific cooperation program between the Federal University of Santa Catarina and EMBRACO. The authors are also grateful to the Brazilian governmental agency CNPq (National Council of Research) for the grants 573581/2008-8 (National Institute of Science and Technology in Refrigeration and Thermophysics) and 141513/2012-8.

## References

[1] Cavallini A, Doretti L, Longo G A, Rosseto L, Bella B and Zannerio A 1996 Thermal analysis of a hermetic reciprocating compressor *Proc. Int. Compress. Eng. Conference at Purdue*. West Lafayette, USA, 535- 540.

[2] Todescat M L, Fagotti F, Prata A T and Ferreira R T 1992 Thermal energy analysis in reciprocating hermetic compressors *Proc. Int. Compress. Eng. Conference at Purdue* West Lafayette, USA, 1419-28.

[3] Birari Y V, Gosavi S S and Jorwekar P P 2006 Use of CFD in design and development of R404a reciprocating compressor *Proc. Int. Compress. Eng. Conference at Purdue*. West Lafayette, USA, C072.

[4] Ooi K T 2003 Heat transfer study of a hermetic refrigeration compressor *Appl. Therm. Eng.* **23** 1931-45.

[5] Sanvezzo Jr. J and Deschamps C J 2012 A heat transfer model combining differential and integral formulations for thermal analysis of reciprocating compressors *Proc. Int. Compress. Eng. Conference at Purdue* West Lafayette, USA, 1-11.

[6] Rigola J, Pérez-Segarra C D and Oliva A 2000 Advanced numerical simulation model of hermetic reciprocating compressors. Parametric study and detailed experimental validation *Proc. Int. Compress. Eng. Conference at Purdue* West Lafayette, USA, 23-30.

[7] Dutra T and Deschamps C J 2014 Development of a lumped-parameter model for hermetic reciprocating compressor with thermal-electrical coupling *Proc. Int. Compress. Eng. Conference at Purdue* West Lafayette, USA, 1367.

[8] He Z, Xing Z, Chen W and Wang X 2013 Thermal and hydraulic analysis on the flow around the motor in semi-hermetic twin screw refrigeration compressors *Appl. Therm. Eng.* **58** 114-124.

[9] Mantri P, Bhakta A, Mallampalli S, Hahn G and Kusumba S 2014 Development and validation of integrated design framework for compressor system model *Proc. Int. Compress. Eng. Conference at Purdue* West Lafayette, USA, 1153.

[10] Link R and Deschamps C J 2011 Numerical modeling of startup transients in reciprocating compressors *Int. J. Refrigeration* **34** 1398-1414.

[11] Mellor P H, Roberts D and Turner D R 1991 Lumped parameter thermal model for electrical machines of TEFC design *IEEE Proc.-B* **138** 205-218.

[12] Boglietti A, Cavagnino A, Lazzari M and Pastorelli M 2003 A simplified thermal model for variable-speed self-cooled industrial induction motor *IEEE Transactions on Industrial Applications* 945-952

[13] Bouafia M, Ziouchi A, Bertin Y and Saulner J B 1999 Experimental and numerical study of heat transfer in an annular gap without axial flow with a rotating inner cylinder *Int. J. Thermal Sciences* **38** 547- 559.

[14] Fitzgerald A E, Kingsley C K and Umans S D 2003 *Electric Machinery* sixth ed. (McGraw-Hill Companies, Inc).

[15] Stepina J 2003 *Single-Phase Induction Motors: Construction, Theory and Calculation* (Motorsoft, Inc).

[16] Arora J S 2004 *Introduction to Optimum Design* second ed. (Elsevier Academic Press).